Nanoelectronics and Its New Materials – A NEW ERA OF NANOSCIENCE

Nanoelectronics and Its New Materials –
A NEW ERA OF NANOSCIENCE

ZEISS
Seeing beyond

WILEY

Discover the recent advances in electronics research and fundamental nanoscience.

Nanotechnology has become the driving force behind breakthroughs in engineering, materials science, physics, chemistry, and biological sciences. In this compendium, we delve into a wide range of novel applications that highlight recent advances in electronics research and fundamental nanoscience. From surface analysis and defect detection to tailored optical functionality and transparent nanowire electrodes, this eBook covers key topics that will revolutionize the future of electronics.

To get your hands on this valuable resource and unleash the power of nanotechnology, simply download the eBook now. Stay ahead of the curve and embrace the future of electronics with nanoscience as your guide.

ZEISS

Seeing beyond

WILEY

Biomimetic Tendrils by Four Dimensional Printing Bimorph Springs with Torsion and Contraction Properties Based on Bio-Compatible Graphene/Silk Fibroin and Poly(3-Hydroxybutyrate-*co*-3-Hydroxyvalerate)

Carmelo De Maria, Irene Chiesa, Davide Morselli, Maria Rachele Ceccarini, Silvia Bittolo Bon, Micaela Degli Esposti, Paola Fabbri, Antonino Morabito, Tommaso Beccari, and Luca Valentini*

Taking inspiration from plant tendril geometry, in this study, 4D bimorph coiled structures with an internal core of graphene nanoplatelets-modified regenerated silk and an external shell of poly(3-hydroxybutyrate-*co*-3-hydroxyvalerate) are fabricated by 4D printing. Finite element simulations and experimental tests demonstrate that integrating these biomaterials with different coefficients of thermal expansion results in the temperature induced self-compression and torsion of the structure. The bimorph spring also exhibits reversible contractive actuation after exposure to water environment that paves its exploitation in regenerative medicine, since core materials also have been proven to be biocompatible. Finally, the authors validate their findings with experimental measurements using such springs for temperature-mediated lengthening of an artificial intestine.

1. Introduction

In nature, plants such as cucumber tendrils show complex motion modes including twisting and contraction in response to environmental conditions.[1–4] The key mechanism of the coiling observed in such plants lies in the internal strain mismatch within the tendril tissues.[5,6] This challenging aspect was partially copied by materials scientists by introducing a prestrain mismatch between two synthetic materials to get a coiled geometry.[7] Helical carbon nanotube fibers as well as polystyrene and polyvinylidene fluoride helical fibers were extensively used for this purpose to fabricate twisting fibers.[8–19] However, to the best of our knowledge, additive manufacturing (AM) technologies were not yet investigated to fabricate such complex structures. AM technologies, commonly known also as "3D printing," are a group of computer aided manufacturing technologies that allow the fabrication of complex structures by the precise and spatially controlled deposition of material, starting from a digital model.[20,21] AM technologies allows to simultaneously deposit multiple materials, thus

C. De Maria, I. Chiesa
Department of Information Engineering and Research Center
E. Piaggio
University of Pisa
Largo Lucio Lazzarino 1, Pisa 56122, Italy
D. Morselli, M. Degli Esposti, P. Fabbri
Department of Civil, Chemical, Environmental and Materials
Engineering (DICAM)
Università di Bologna
Via Terracini 28, Bologna 40131, Italy
D. Morselli, S. Bittolo Bon, M. Degli Esposti, P. Fabbri, L. Valentini
National Interuniversity Consortium of Materials Science
and Technology (INSTM)
Via Giusti 9, Firenze 50121, Italy
E-mail: luca.valentini@unipg.it

The ORCID identification number(s) for the author(s) of this article can be found under https://doi.org/10.1002/adfm.202105665.

M. R. Ceccarini, T. Beccari
Department of Pharmaceutical Sciences
University of Perugia
Perugia 06123, Italy
S. Bittolo Bon, L. Valentini
Dipartimento di Ingegneria Civile e Ambientale
Università degli Studi di Perugia
Strada di Pentima 4, Terni 05100, Italy
A. Morabito
Department of Pediatric Surgery
Meyer Children's Hospital
Viale Pieraccini 24, Firenze 50139, Italy
A. Morabito
Dipartimento Neuroscienze, Psicologia, Area del Farmaco e della Salute
del Bambino NEUROFARBA
Università degli Studi di Firenze
Viale Pieraccini 6, Firenze 50121, Italy

**ADVANCED
SCIENCE NEWS**
www.advancedsciencenews.com

**ADVANCED
FUNCTIONAL
MATERIALS**
www.afm-journal.de

boosting the fabrication of multimaterial and hierarchical structure, including bilayers and coiled multimaterial 3D structures.[22]

To produce tendril-like structures it is important to design structures able to self-transform in accordance with external stimuli, such as temperature and humidity. Different coefficients of thermal expansion (α) between polymers within a 3D structure can induce a controlled shape-shifting at low thermal stimulation.[23–26] Natural-based polymers would pave their exploitation in self-shaping structures for distraction enterogenesis, hypothesizing self-contracting spring that provides the tissue lengthening and triggers cellular proliferation.[27–29] In this regard, a recent work of Dunn et al.,[30] starting from previous studies where a spring, with a constant ≈7 N m^{-1} exerting a force of 0.46 N, was used to lengthen porcine small intestinal segments, demonstrated that springs, with constants of at least 2 N m^{-1} exerting a minimum force of 0.10 N, significantly lengthened intestinal segments. They conclude that a reduced force can induce spring-mediated distraction enterogenesis.

The use of such smart materials as inks for AM to fabricate shape-transform structures has been defined as 4D printing.[31–33] In 4D printing, AM technologies are exploited to fabricate structures whose properties and/or shape change in time in a programmable way under a predefined stimulus. 4D printing is influenced by several variables (e.g., stimulus, materials, and geometries), thus mathematical models are a very useful tool to identify the combination of variables that leads to the maximum and desired movement.[34]

On the basis of previous studies,[23,24] natural polymers, such as regenerated silk (RS) ($\alpha = -4 \times 10^{-4}$ °C^{-1}) and poly(3-hydroxybutyrate-co-3-hydroxyvalerate) (PHBV, $\alpha \approx 2 \times 10^{-4}$ °C^{-1}) could represent a suitable materials combination for 4D printing bimorph shape-changing and self-contracting structures, which could be exploited in tissue engineering to trigger cellular functions and to provide tissue lengthening in distraction enterogenesis.[27–30]

In this work, we optimize a one-step AM process to fabricate 4D tendril-like structure, composed of an internal core of biocompatible graphene nanoplatelets (GNPs)-modified RS and an external shell of PHBV to obtain torsional and contractile actuators. The mechanical properties of the structures were tuned by the addition of graphene to the RS with different calcium ions content. The different coefficient of thermal expansion of RS and PHBV succeeds in converting thermal energy into mechanical torsion and contraction. Furthermore, the bimorph spring also exhibits reversible contractive actuation after exposure to the water environment. Finite element (FE) simulations were exploited to study the thermal-induced shape-morphing behavior of the structures. Finally, after proving the biocompatibility of the constituent materials, this programmable motility was used in a practical task of regenerative medicine such as a spring-mediated actuator for lengthening an artificial intestine.

2. Experimental Section

2.1. Materials Preparation

Silk cocoons were supplied from local farm. Sodium hydrogen carbonate (NaHCO$_3$), calcium chloride (CaCl$_2$), formic acid (FA), chloroform (CHCl$_3$), potassium nitrate (KNO$_3$), PHBV custom grade,

and Pluronic acid F127 were supplied by Sigma-Aldrich. GNPs C777 (carbon content > 65%, average flake thickness ≈ 20 nm, layer number ≈ 41, average particle [lateral] size = 16 µm, [Figure S1, Supporting Information]) were supplied by Nanesa.

Silk cocoons were degummed with NaHCO$_3$ (5 g in 200 mL of water) in boiling water for 30 min and rinsed with deionized water; the procedure was repeated two times. The degummed fibers were then left for drying at room temperature.

RS solutions for 3D printing was produced by dispersing the degummed silk fibers into the FA/CaCl$_2$ solution by magnetic stirring at room temperature for 5 min to obtain a homogeneous solution; CaCl$_2$ amount was calculated with different silk:CaCl$_2$ weight ratios (i.e., 80:20 and 60:40) with respect to the silk amount (0.65 g) and it was dissolved in FA (5 mL). Afterward, 3.5 wt% of KNO$_3$ was added to the solution, leaving the reaction to proceed (≈30 min.) until a brown color was obtained. KNO$_3$ was added to increase the amount of β-sheet and, as a consequence, to enhance material mechanical properties, as the authors previously showed.[24] Finally, 1 wt% of GNPs were added to the solutions and stirred for 30 min at room temperature. Hereinafter, the authors referred to RS/GNPs for samples obtained by using GNPs dispersed in RS. PHBV was purified as described elsewhere,[26] and dissolved in CHCl$_3$ with a final concentration of 150 mg mL^{-1}. An 18% w/v solution of Pluronic acid F-127 in deionized water was prepared by the previously described "hot technique."[35]

2.2. Four-Dimensional Printing Process

Core–shell coiled 3D structures (3D digital model and the printing preview are shown in **Figure 1**A,B, respectively) were 4D printed with an extrusion-based 3D printer equipped with two piston-driven extruders and a coaxial needle (Ramé-hart instrument co., United States, internal needle diameter 23G, external needle diameter 17G) (Figure 1C). Geometrical dimensions of the structure are reported in Figure 1A; the GCODE to achieve the desired structure was generated using online tools and manually adapted.[36] The PHBV solution was used as shell ink for all the structures, whereas four different RS compounds were used as core ink: i) 60:40 RS; ii) 60:40 RS/GNPs; iii) 80:20 RS; and iv) 80:20 RS/GNPs. Due to the low viscosity of the inks and the complex geometry of the desired structure, the coils were printed into a sacrificial support material of Pluronic acid (bioplotting technique[21,37]) (Figure 1D,E). After printing, the tendril-like structures were kept into the support material overnight to allow the complete diffusion of the solvents (i.e., chloroform and formic acid) into the Pluronic hydrogel. This determined the formation of a solid structure due to phase inversion.[38] They were then placed at 4 °C for 2 h to liquefy the Pluronic acid, and finally washed in deionized water to eliminate the support leftover. Finally, in order to remove any solvent leftover from the tendril-like structures, they were dried at room temperature for 24 h.

2.3. Finite Element Analysis of the Shape Morphing Behavior of Tendril-Like Structure

FE models were implemented in Comsol Multiphysics (Comsol Inc., 5.3) to analyze the temperature-controlled shape-morphing
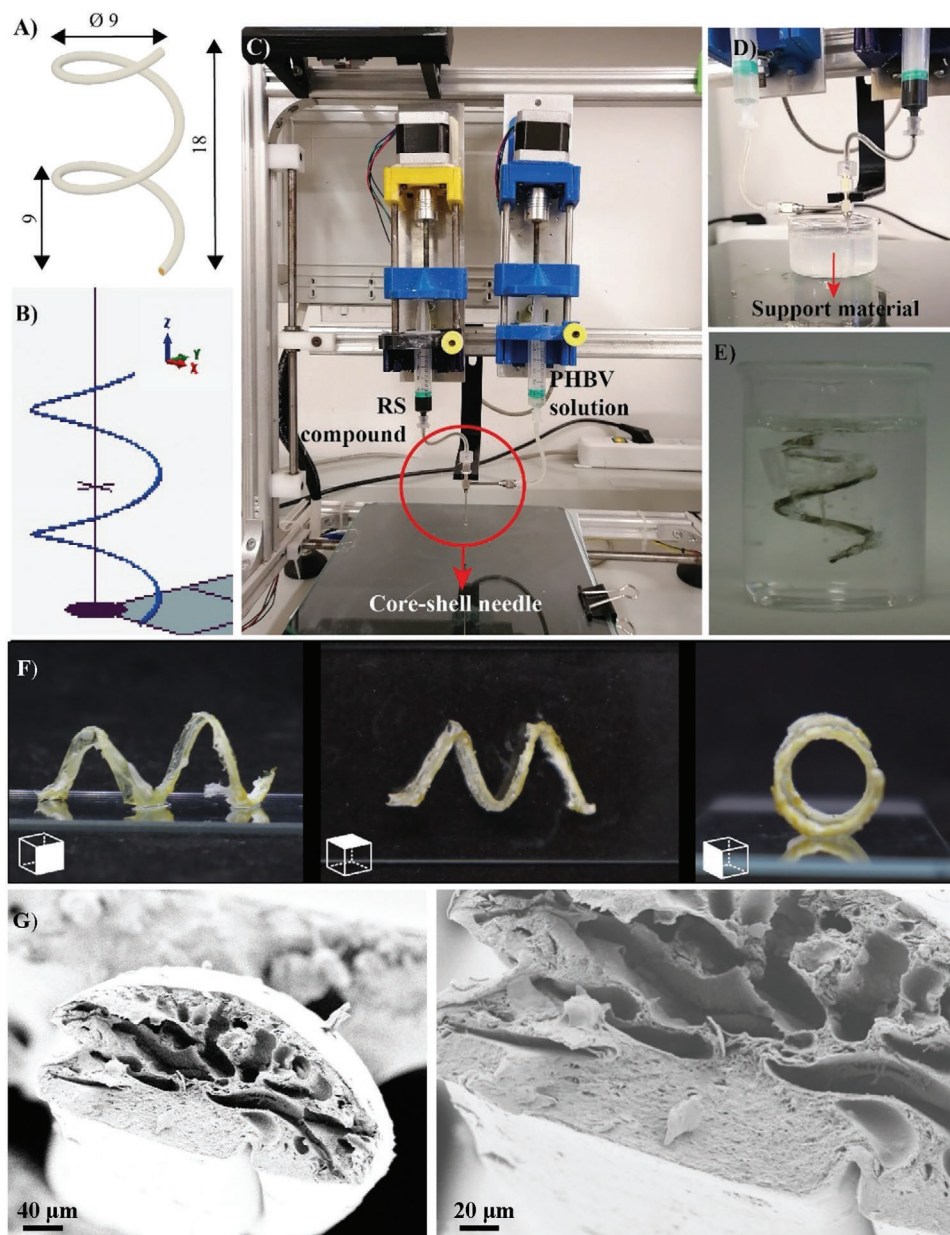
Figure 1. A) 3D compuer aided design model of the tendril-like structure with geometrical dimensions in mm, whose core is made of a RS compound and the shell of PHBV. B) Printing preview of the structure. C) Piston-driven extrusion-based 3D printer equipped with two extruders and a coaxial needle used in all the experiments. D) Bioplotting technique, that is, the materials are extruded into a sacrificial support material. E) Core–shell tendril-like structure into the support material immediately after the printing process. F) Frontal, top, and lateral view of 4D printed tendril-like structure once retrieved from the support material. G) FESEM images of the structures, where the core–shell structure is clearly visible. Scale bars indicate 40 and 20 μm, respectively.

behavior of 4D printed tendril-like structure, due to the negative thermal expansion coefficient of the RS compounds. In all simulations, the solid mechanics application mode in static condition was used. 3D models were designed in the software with the dimensions reported in Figure 1A. Images taken with field emission electron microscopy (FESEM) (described in the next paragraph) were used to get the diameter of the shell and core sections, approximately equal to 700 and 550 μm, respectively. In all subdomains, a linear elastic material model was

used, with the addition of the thermal expansion model. The shell subdomain was always set as PHBV, whereas each RS compound was used as core subdomain (four combinations in total). Subdomain settings are reported in **Table 1** and were derived as described in Table S1, Supporting Information. A body load due to gravity was set in all domains. The strain reference temperature was set as 20 °C, whereas the working temperature was set at 37 °C (i.e., physiological temperature). Then, two different models were implemented. The first one aimed to

**ADVANCED
SCIENCE NEWS**

www.advancedsciencenews.com

**ADVANCED
FUNCTIONAL
MATERIALS**

www.afm-journal.de

Table 1. Subdomain settings implemented into the FE simulation. Young's modulus values were derived from Figure S2, Supporting Information. The error for the experimental values of the thermal expansion coefficient is 12%.

	PHBV	RS 60:40	RS/GNPs 60:40	RS 80:20	RS/GNPs 80:20
Young's modulus [MPa]	565	354	578	902	1083
Density [kg m^{-3}]	1230	1066	1022	1099	1053
Poisson coefficient [–]	0.4	0.4	0.4	0.4	0.4
Thermal expansion coefficient [K^{-1}]	2.0E-4	−4.0E-4	−1.9E-3	−4.0E-4	−3.7E-3

calculate the elastic spring constant of the structures, whereas the second one aimed to evaluate the temperature-induced self-contraction and torsion behavior of the structure.

2.3.1. Elastic Spring Constant Evaluation

Subdomain settings are described above, and boundary conditions are reported in **Figure 2**A,B. Briefly, one end of the structure was fixed, whereas on the other end an edge load equal to a 2.8 g mass was set along the z-axis, that corresponds to the spring axis. In this model the thermal expansion module was disabled, to explore the elastic spring constant without the effect of the temperature-induced movements. A triangular mesh, controlled by the physics, was used in all the simulations. Mesh statistics are shown in Table S1, Supporting Information. Then, the displacement field along the z-axis was evaluated in point P (inset of Figure 2B). Finally, the elastic spring constant k [N m^{-1}] was obtained as per Equation (1) for each RS compound:

$$k = \frac{applied\ force}{displacement\ along\ z-axis} \tag{1}$$

2.3.2. Temperature Induced Torsion and Compression Behavior of the Four Dimensional Printed Structure

Subdomain settings are described above, and boundary conditions are reported in Figure 2A. More in detail, one end of the structure was fixed, whereas all the other boundaries were set as free. A triangular mesh, controlled by the physics, was used in all the simulations. Mesh statistics are the same as above, shown in Table S1, Supporting Information. Then, the total displacement of point P and the displacement field along x, y, and z axes of point P were evaluated to summarize the capability of the 4D printed tendril-like structure to compress and twist at physiological temperature.

2.4. Characterizations

Fourier transform infrared (FTIR) investigations were carried out on a PerkinElmer Spectrum Two spectrometer equipped with a diamond crystal in attenuated total reflectance mode. Measurements were performed in the range of 4000–400 cm^{-1} at room temperature; the spectral resolution was 4 cm^{-1} and the number of scans was 64 for each spectrum. Spectral data were processed with Spectrum 10 software (PerkinElmer). The sample was carefully disassembled by a very fine surgical scalpel and with the help of magnification lens and optical stereo microscope (SZX10, Olympus). Specifically, a small portion of the coil (≈10 mm) had been fixed on a microscope glass and sectioned as longitudinally as possible. Afterward, the RS core was carefully removed from the shell to obtain two samples. The RS core and both sides of the PHBV shell were analyzed by FTIR. The sectioned tendril structure was also analyzed in the range of 1750–1520 cm^{-1} that were the amide I and amide II bands of RS. The signal recorded between 1100 and 1400 cm^{-1} as well as the peak at 1713 cm^{-1} were attributed to
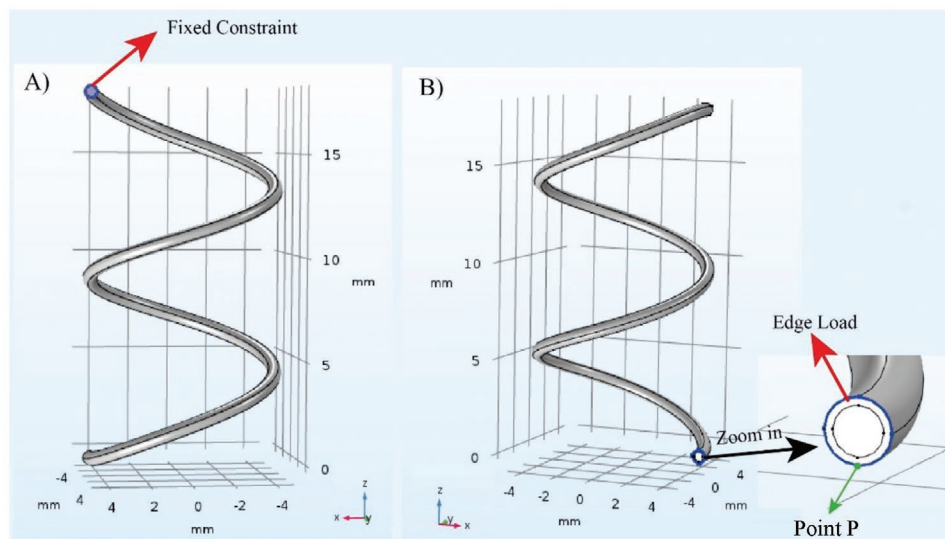

Figure 2. Boundary conditions of the FE simulations. In the first model (i.e., evaluation of the elastic spring constant, paragraph 2.3.1.) one end of the structure was fixed (A); whereas an edge constraint was imposed on the other end (B). All the other boundaries were set as free. Differently, in the second model (i.e., evaluation of the temperature induced self-contraction and torsion behaviour, paragraph 2.3.2.) one end of the structure was fixed (Fixed constraint, A); whereas all the other boundaries were imposed as free.

2105665 (4 of 13)

**ADVANCED
SCIENCE NEWS**

www.advancedsciencenews.com

**ADVANCED
FUNCTIONAL
MATERIALS**

www.afm-journal.de

the PHBV layer.[39] The spectra were then deconvoluted by first smoothing the signal with a polynomial function with a 15-point Savitski–Golay smoothing function, subtracting a linear baseline, and applying Gaussian deconvoluting curves by Origin 9 software.

The samples were analyzed by FTIR before and after irradiation with a germicidal ultraviolet (UV) light. The material treatment was performed using an UV-C SANKIO DENKI G15T8 lamp with an irradiation wavelength centered at 253.7 nm (UV output = 4.9 W), mounted into a cabinet model SafeFAST Classic 212, DASITgroup. Specimens were placed at 60 cm apart from UV source and irradiated for 20 min each side.

Thermal properties of the springs specimens were analyzed by differential scanning calorimetry (DSC, Q10, TA Instruments) equipped with a Discovery Refrigerated Cooling System (RCS90, TA Instruments). Approximately 5 mg of each sample were placed into aluminum pans and subjected to two heating cycles from –60 to +200 °C with a heating rate of 5 °C min^{-1}. The DSC cell was purged with dry nitrogen at 50 mL min^{-1}. Before the measurements, the system was calibrated both in temperature and enthalpy with indium standard. DSC curves were processed with TA Universal Analysis 2000 software (TA Instruments) in order to extrapolate the glass transition temperature (T_g) from the typical enthalpic jump associated to the transition from the glassy to rubbery state. T_g was determined as the mean value between the onset-point and end-point of the typical signal associated with the glass transition. Each T_g values and associated standard deviations were the result of triplicate DSC measurement.

The morphology of the 4D coiled structures was investigated by FESEM (Supra 35). Before imaging, the cross section of the tendrils was sputtered with a 2 nm layer of gold.

The stress–strain curves of the coiled structures were obtained through a tensile testing machine (Lloyd Instr. LR30K, UK). The samples were tested at room temperature with a strain rate of 5 mm min^{-1} using a 500 N load cell. Three samples per composition were tested.

Then, the temperature-induced torsion of the tendril-like structures was investigated. More in detail, the torsion was monitored by clamping a paddle with 2 mg weight at one end of the spring and leaving it free to rotate until it was balanced. A video camera was fixed right above the specimen to record the temperature-induced torsion of the structure, from 25 to 37 °C. A heater was positioned 30 cm apart from the specimen and the temperature was recorded on the spring with an infrared thermometer. An image processing program was used to determine the rotation of the paddle (see Supporting Information).

The humidity-induced contraction properties were observed by fixing the ends of the spring to the dynamometer grips and giving a prestrain (below 1%). Then, the grips were inserted into a chamber with a relative humidity of 90% at room temperature for 20 min. Then the samples were removed from the chamber. The load was monitored as a function of the time.

The phantom intestine was made of commercial platinum-catalyzed silicone, Ecoflex 00-10 (tensile strength = 120 psi, 100% modulus = 8 psi, elongation at break = 800%, shore hardness 00–10; inner diameter = 30.0 ± 0.1 mm and outer diameter = 32.0 ± 0.1 mm).

2.5. Cytotoxicity Assay In Vitro of the Core Compounds

HepG2 cell line, purchased from ATCC (ATCC HB 8065), was used as a representative model to appreciate the biocompatibility of the core compounds. HepG2, a human hepatocyte carcinoma, had been cultured according to standard procedures[40] in Eagle's minimum essential medium, supplemented with 10% heat-inactivated fetal bovine serum, 1% non-essential amino acids, 1 mM sodium pyruvate, 2 mM of L-glutamine, and antibiotics (100 U ml^{-1} penicillin, 100 µg mL^{-1} streptomycin). The cells were maintained in a cell incubator at 37 °C in humidified atmosphere containing 5% CO$_2$. HepG2 cells were subcultured by dispersal with 0.05% trypsin in 0.02% ethylenediaminetetracetic acid tetrasodium salt (Na$_4$EDTA) for a contact time of 5 min and seeded at a 1:3 dilution, which maintained cells in the exponential growth phase. The cellular viability and cytotoxicity of various compounds were assessed using 3-(4,5-dimethylthiazol-2-yl)-2,5-diphenyltetrazolium bromide (MTT) assay after 24 and 48 h of treatment.[41] HepG2 cells were seeded in a 96-well plate at 1×10^4 cells/well final cell density. After 24 h, fresh complete medium was replaced with different treatments. The stock solutions (1 mg mL^{-1}) were prepared incubating the four compounds (RS 60:40, RS/GNPs 60:40, RS 80:20, and RS/GNPs 80:20) with complete medium for 1 h at 37 °C. For each compound six scalar dilutions were tested (1, 0.5, 0.25, 0.125, 0.0625, and 0.03125 mg mL^{-1}) after 24 and 48 h of incubation. 24 different combinations were obtained; the 1 mg mL^{-1} was the only stock solution, the 0.5 mg mL^{-1} was obtained by diluting the stock solution 1:1 with complete medium, the 0. 25 mg mL^{-1} was diluted 4 times with complete medium, the 0.125 mg mL^{-1} was the result of 8 times dilution, the 0.0625 mg mL^{-1} was diluted 16 times, and finally the 0.03125 mg mL^{-1} was diluted 32 times. MTT reagent (0.5 mg mL^{-1} in PBS 1X) was added in each well at 0.05 µg µL^{-1} final concentration for 3 h at 37 °C. Then, the supernatant was carefully removed, and formazan salt crystals inside cells were dissolved in 100 µL DMSO 100% and the OD values were measured spectrophotometrically at 570 nm (Eliza MAT 2000, DRG Instruments GmbH, Marburg, Germany). Each experiment was performed in triplicate for three times and cell viability was expressed as a percentage relative, as previously described.[42]

2.6. Statistical Analysis

Values were represented as mean ± standard deviation and were compared with one-way ANOVA with $p \leq 0.05$ considered statistically significant; *$p < 0.01$, **$p < 0.001$, and ***$p < 0.0001$.

3. Results and Discussion

3.1. Four-Dimensional Printing of Multimaterial Bio-Based Tendril-Like Structures

The designed concept of this work lies in the incorporation of a temperature responsive RS core into a biopolymer external shell made of PHBV, able to preserve the RS from the environmental humidity. To achieve this goal, we exploited an

**ADVANCED
SCIENCE NEWS**
www.advancedsciencenews.com

**ADVANCED
FUNCTIONAL
MATERIALS**
www.afm-journal.de

extrusion-based 3D printer featuring a core–shell needle, to simultaneously deposit PHBV and RS compounds in a 3D tendril-lake structure. More in detail, bioplotting technique (Figure 1A–E and Movie S1, Supporting Information)[36,37] allowed to obtain self-supporting, customizable, and highly reproducible tendril-like structures, with an inner core of a RS compound (a total of different four compounds tested) and the wrapping layer made of PHBV. Images of the obtained tendril-like structures are reported in Figure 1F. FESEM analysis of the cross section of the 4D printed tendril-like structures (Figure 1G) reveals the coaxial structure (thickness of ≈0.7 mm) with the helical RS fiber (thickness of ≈0.6 mm), embedded into the PHBV layer.

When pure PHBV or pure RS compounds were printed separately, it is not possible to obtain a stable structure differently from the coaxial structure shown in Figure 1F. When the sole PHBV is deposited, interfacial forces that arise due to the immiscibility of PHBV and Pluronic acid, destabilize the printed line through a mechanism similar to the Plateau–Rayleigh (PR) instability.[43] This leads to the breakage of the deposited PHBV line into separated drops, as can be seen in **Figure 3**A and Movie S2, Supporting Information. On the other hand, when the sole RS/GNPs compound is deposited, a phase separation occurs between RS and GNP, thus leading to the agglomeration of the RS (red circle) in the upper part of the structure (Figure 3B). Consequently, the use of a coaxial needle to simultaneously deposit the PHBV and the RS compound allows to stabilize the structure and to successfully fabricate a tendril-like structure, avoiding the PR instability as well as the phase separation of the RS/GNP compound. It can be speculated that, on one side, the PHBV encapsulates and preserves the RS/GNP compound and, on the other side, the addition of a RS core decreases the destabilizing interfacial forces between PHBV and Pluronic acid.
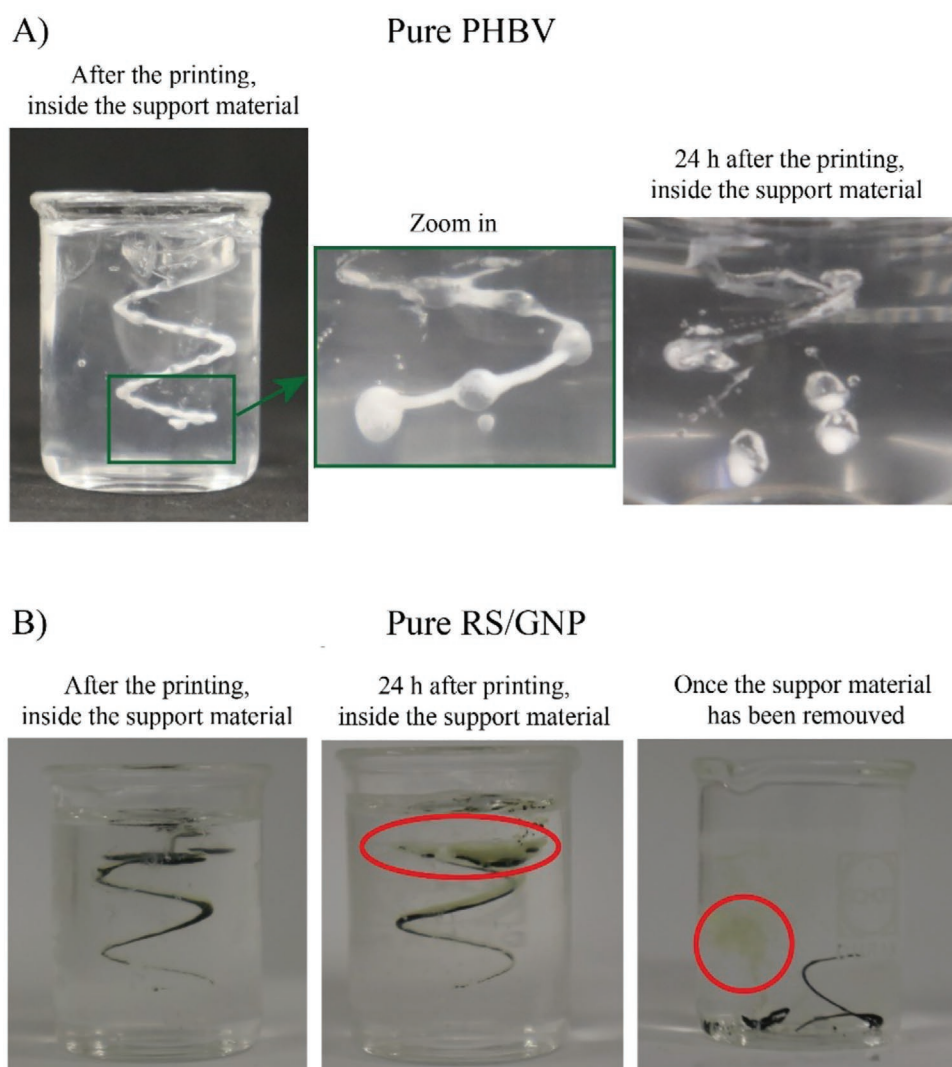

Figure 3. Trials of 3D/4D printing tendril-like structure made of A) pure PHBV and B) pure RS compound. Both trials failed. On one hand, the PR instability between PHBV and Pluronic acid leads to the breakage of the printed PHBV line into single drops over time. On the other hand, the RS/GNP compound underwent a phase separation 24 h after the printing, thus leading to the failure of the structure. Red circles highlight the RS phase that is separated from the GNP over time.

Moreover, when the two materials are simultaneously printed the shell is not only composed of bare PHBV, but also by a PHBV/RS blend. As shown by FTIR spectra reported in **Figure** 4A, the two most typical signals of RS (in the range 1600–1700 cm^{-1}) appear in the spectra of the closest PHBV layer to the RS core (FTIR assignments of PHBV and RS are reported in Supporting Information). It is noteworthy that the incorporation of RS results in a plasticization effect of the PHBV, significantly reducing its T_g, as shown by the DSC curves reported in Figure 4B. On the other hand, the incorporation of GNPs leads to a slight increase of the T_g (≈2–3 °C) due to the constrained polymer chain mobility as previously described elsewhere.[44–46] Specifically, neat PHBV shows a T_g of −3.2 ± 0.4 °C, which decreases to −14.9 ± 0.9, −12.2 ± 0.7, −11.8 ± 0.8, and −9.8 ± 0.7 °C for PHBV-RS 60:40, PHBV-RS/GNPs 60:40, PHBV-RS 80:20, and PHBV-RS/GNPs 80:20, respectively. As

shown in Figure 4C, the T_g increase due to the addition of GNPs is significantly lower than the lowering effect due to RS, leading to an overall plasticization for all samples.

This plasticization effect is in accordance with the observed improved printability of the PHBV solution when it is simultaneously printed with the RS solution. Probably, RS partially diffuses into the PHBV layer during the process, inducing a plasticization effect and stabilizing the interactions at the interface of PHBV-printed lines and Pluronic acid.

3.2. Finite Element Simulation of Temperature-Induced Self-Contraction and Torsion Behavior of the Tendril-Like Structures

FE simulations were implemented to study the actuation properties of the 4D printed tendril-like structures as the RS
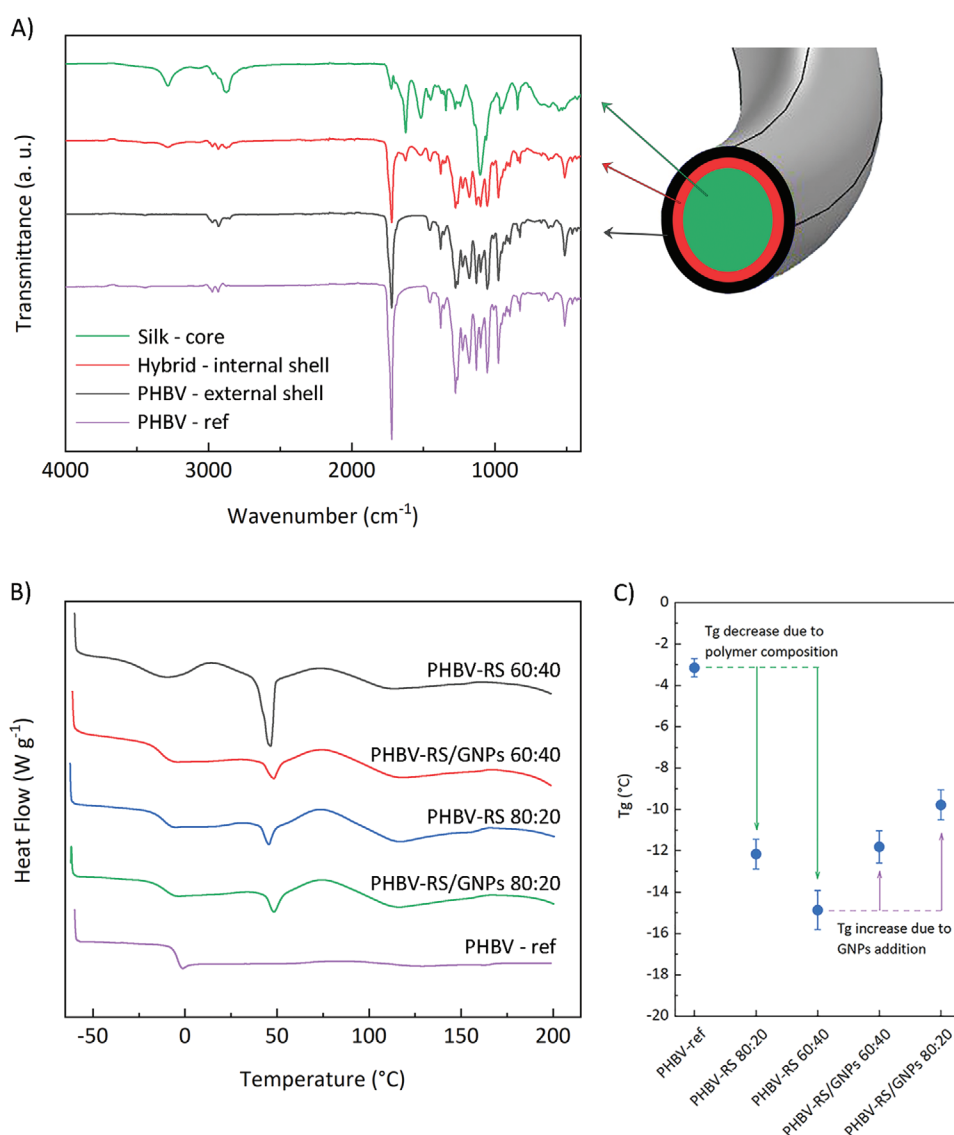

Figure 4. A) Schematic representation of the spring cross section and associated FTIR spectra of the RS core and PHBV wrapping layer of the printed structure. B) DSC thermograms of all prepared samples and neat PHBV as reference. C) Glass transition temperature (T_g) variation as a function of the sample formulation.

2105665 (7 of 13)

**ADVANCED
SCIENCE NEWS**

www.advancedsciencenews.com

**ADVANCED
FUNCTIONAL
MATERIALS**

www.afm-journal.de

Table 2. Results obtained from the FE models. Tendril-like structures have an elastic spring constant around 2 N m^{-1}, that increases with the Young's modulus of the RS compound, and show both self-contraction and torsion when temperature arises (from room temperature to body temperature). The self-contraction (displacement field along z-axis) arises as the Young's modulus and the coefficient of thermal contraction of the RS compound arise.

Core RS compound	Elastic Spring Constant [N m^{-1}]	Total displacement [µm]	Displacement field, fixed point [µm]		
			x-axis	y-axis	z-axis
RS 60:40	1.7	123	11	−120	21
RS/GNPs 60:40	1.9	418	16	−210	361
RS 80:20	2.3	74	6	−56	48
RS/GNPs 80:20	2.5	845	10	−149	834

compound varies. First, the elastic spring constant (k) was evaluated as described in the Section 2.3.1 for all RS compounds. As shown in **Table 2**, for all samples, a k value around 2 N m^{-1} was obtained. As expected, the k increases with the increase of the Young's modulus of the RS compound. Then, the self-contraction and torsion capability of the structure was evaluated analyzing the displacement field in each direction (Table 2) induced by a temperature variation (i.e., from room temperature to body temperature). As expected, a greater contraction (i.e., movement along z-axis that corresponds to the spring axis) is obtained when the 80:20 RS/GNP compound is simulated (Table 2 and **Figure 5**), due to its higher Young's modulus and thermal contraction coefficient. Notably, the end point of the structure self-moves not only along the z-axis but also along the x- and y-axis (Table 2 and Figure 5), thus proving a temperature-induced self-contraction and torsion of the structure.

3.3. Structure Characterization

Structural changes of the RS, depending on the calcium chloride content and GNPs addition, were investigated by FTIR spectroscopy. The spectra reported in **Figure 6**A show the amide I and amide II peaks, where the absorptions between

1622 and 1637 cm^{-1} correspond to β-sheet structure, and those at 1650 and 1540 cm^{-1} are indicative of random-coil and α-helical structure, respectively.[47] The ratio of the peak area with respect to the total area was used to estimate the percentage content of secondary structures that are summarized in Figure 6B. According to previous results, neat RS samples obtained with a lower content of calcium chloride show a higher content of β-sheet structure while, for the 60:40 weight ratio, prevalent random coils/alpha conformations were observed (Figure 6B). It is noteworthy that when GNPs are added to the PHBV-RS 80:20 sample, the crystalline fraction of β-sheets remains unaltered and helical structures increase.

The effect of the calcium chloride content and GNPs addition on the tensile properties of the tendrils was also investigated (Figure 6C). The springs exhibited stress–strain intermediate behavior of plastic and an elastomer, while the addition of GNPs increased the achievable maximum strain. The stretch range and spring constant of the prepared coils were also measured and reported in Figure 6D. As the stretch range decreases, the spring constant arises. The analysis of mechanical properties indicates also that the addition of GNPs increases the mechanical strength, with a higher elongation at break and thus with a tougher spring.

The experimental set-up used to investigate the temperature-driven torsion of bimorph springs is reported in **Figure 7**A. A torsional response was obtained at 37 °C for all specimens. The rotation speed was calculated according to the method reported in the Supporting Information. The temperature-induced torsion of springs with different core materials is reported in Figure 7B,C. After the application of the thermal stimulus, no appreciable self-rotation on the PHBV-RS 60:40 spring was observed, while the speed increased to about 70 and 20° min^{-1} for bimorph 60:40 and 80:20 PHBV-RS/GNPs springs, respectively. The change of the length of the springs before and after the application of the weight was measured by the camera, and the engineering strain was found to vary from ≈5% to 10%.

As proof-of-concept of the exploitation of the developed 4D printed tendril-like structures in regenerative medicine, we demonstrated that such springs can be used in lengthening
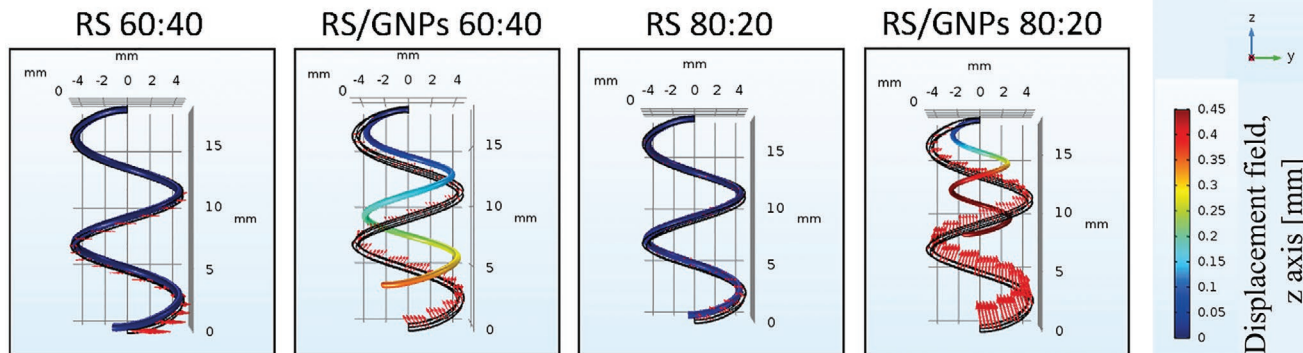

Figure 5. Surface plot of the displacement field along z-axis (mm), on the global deformed shape of the core–shell tendril-like structures, as RS compound varies (deformed shape scale factor equals to 10 for all the figures). Red arrows highlight the direction of the displacement field and show that the structure is characterized by both contraction and torsion (arrow scale factor equals to 15 for RS compounds, and equals to 3 for RS-GNP compounds).
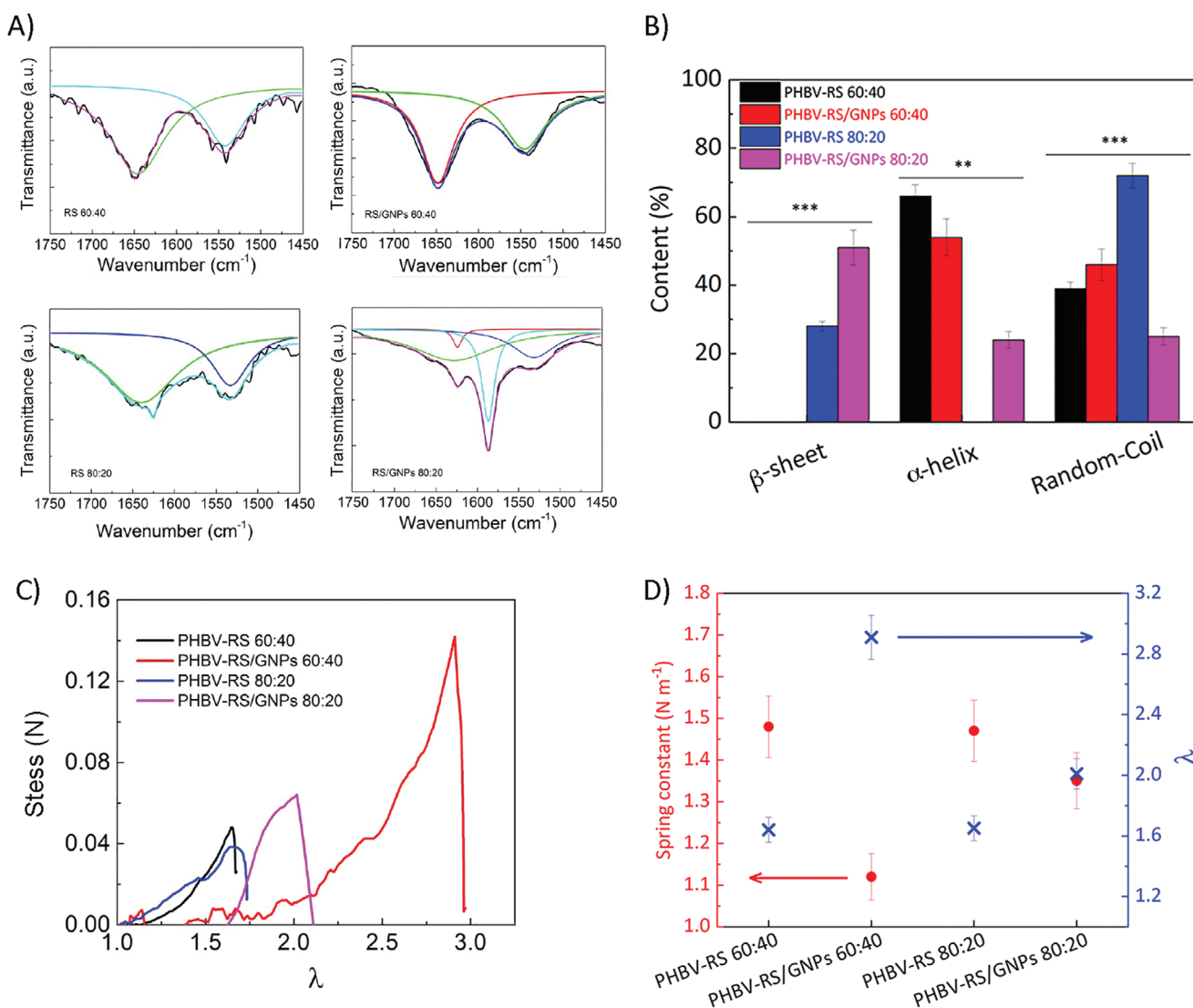
Figure 6. A) FTIR spectra in amide-I and amide II regions of RS and RS/GNPs cores of bimorph springs with different RS:CaCl$_2$ ratios. Peak deconvolution is carried out by peak assignment to the secondary structures: 1650 cm^{-1} (random coils), 1620 cm^{-1} (β-sheet), and 1540 cm^{-1} (α-helices). B) Quantitative analysis of secondary structures in RS 60:40, RS/GNPs 60:40, RS 80:20, and RS/GNPs 80:20, respectively. All data were expressed as mean ± standard deviation and were analyzed using one-way ANOVA. A p-value ≤ 0.05 was considered statistically significant. $**p < 0.001$ and $***p < 0.0001$. C) Stress–strain curves of the prepared springs with different core compositions. D) Stretch ratio at break and spring constant of the prepared coiled structures with different core compositions.

a phantom intestine. Specifically, in Figure 7D and Movie S3, Supporting Information, when the thermal stimulus (i.e., 37 °C) was applied, the PHBV-RS/GNPs 80:20 tendril pulled the flaps of an artificial intestine. Specifically, we observed a contraction from 3.58 to 3.49 cm. Although such differences are minimal, such device could be used to stimulate cell proliferation; indeed, it was reported that the stretch stimulates cellular proliferation and differentiation in intestinal epithelial cells.[48] Interestingly, the stimulation of intestinal epithelial proliferation was found to respond optimally to 10–20 cycles per minute of strain.[49]

Humidity-induced contraction of dragline silk from spider is a well-known effect and has been reported in previous studies.[50,51] On the other hand, the humidity contraction

in RS fibroin is still under investigation. Our samples, both PHBV/RS and PHBV/RS/GNPs, after 20 min of exposure to the humidity show a reduction of the gauge force (Figure 7E,F) as a result of the disruption of the hydrogen bond network found in the dry RS thus showing an elastomeric behavior under wet condition.[52] In contrast, after subsequent drying, all springs show the tendency to recover the original gauge force. This result is in agreement with the paper by Numata et al.,[53] which first demonstrated that by increasing the water content of silk, the water molecules were removed at low temperatures, indicating that the amount of free water in silk materials increased; additionally, their silk films also suggested that the water molecules in the amorphous regions of the silk films acted as a plasticizer and induced β-sheet
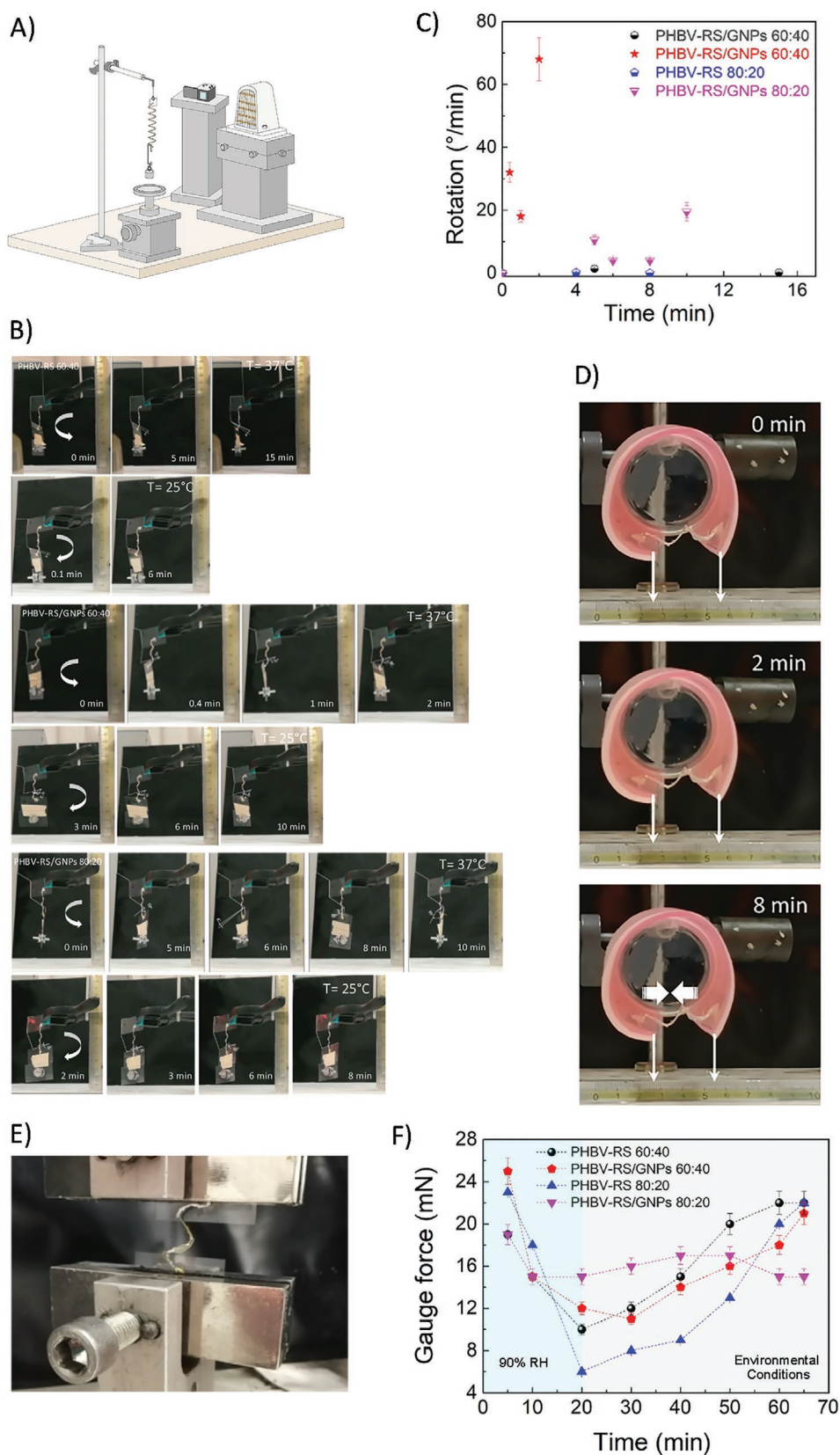
**ADVANCED
SCIENCE NEWS**

www.advancedsciencenews.com

**ADVANCED
FUNCTIONAL
MATERIALS**

www.afm-journal.de

Figure 7. A) Schematic diagram of the apparatus for measuring the mechanical torsion actuation of tendrils driven by the temperature. B) Photographs showing, from top to the bottom, the torsion of PHBV-RS 60:40, PHBV-RS/GNPs 60:40, and PHBV-RS/GNPs 80:20 springs. The arrows indicate the
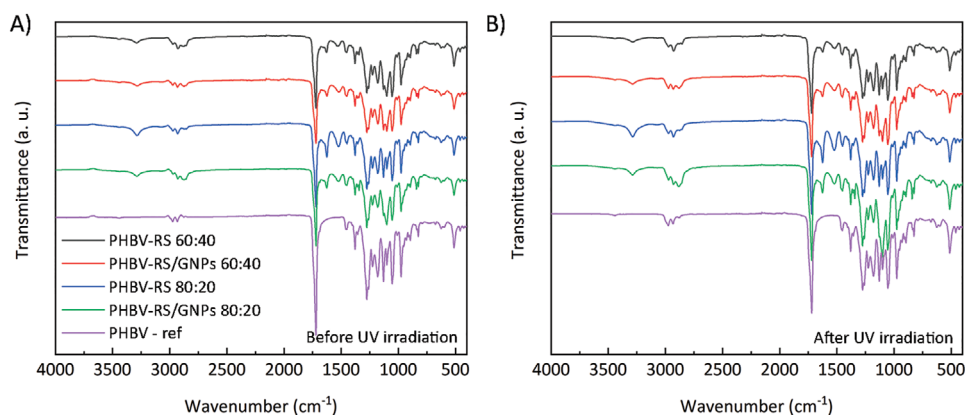
Figure 8. FTIR spectra for all prepared samples and neat PHBV as a reference A) before and B) after the UV-sterilization process.

crystallization. The force generated by the springs connected to a force gauge and obtained as the ratio between the force and the different time intervals during the recovery indicate an actuation rate of 0.016 and 0.040 N s^{-1} for PHBV-RS and PHBV-RS/GNPs springs, respectively.

3.4. Four-Dimensionally Printed Tendril-Like Structure Biocompatibility

Envisioning a biomedical application, the effect of the UV irradiation, as a procedure for maintaining the decontamination and preventing infections[54,55] in the unfortunate case of surface contamination, was investigated. In **Figure 8**A,B the FTIR spectra of the materials that compose the 4D printed structure, before and after the UV irradiation, do not show any significant modification of the chemical structure, indicating that UV treatment is a viable strategy that can be easily performed in the operating room prior to the device implantation.

To evaluate the safety of the core compounds, six scalar concentrations, obtained from stock solution 1 mg mL^{-1}, were tested in vitro using cytotoxicity study (MTT test). Instead, the cytotoxicity of the PHBV shell was addressed elsewhere.[26] This assay is based on the reduction by dehydrogenase enzyme secreted from mitochondrial of the yellow tetrazolium salt, MTT, to purple formazan crystals. Only metabolically active cells are able to do this transformation and the amount of insoluble formazan is proportional to the number of viable cells.[56] Human liver cancer cells (HepG2) were used as model cell system.[40]

The obtained results (**Figure 9**A,B) show that these compounds (i.e., RS 60:20, RS/GNPs 60:40, RS 80:20 and RS/GNPs 80:20) are completely safe for the cells after 24 h of treatment with cell viability ≥ 80%. A low cytotoxic effect was observed only after 48 h in a dose-dependent manner for the RS/GNPs 80:20 at the highest concentrations assayed, namely 0.5 mg mL^{-1} (viability < 80%) and 1 mg mL^{-1} (viability < 70%).

Based on MTT results and repeated after one week of soaking (Figure 9 and Figure S3, Supporting Information), it is possible to conclude that new bimorph structures are noncytotoxic for the human cells. Hence, these materials could be considered suitable for tissue engineering applications.

4. Conclusions

Taking inspiration from the coiling mechanism in plant tendrils, we 4D printed a core–shell bio-based tendril-like structure, by simultaneously depositing a silk fibroin core into a bio-degradable PHBV shell. Thanks to the proper spatial arrangement of the selected materials, the fabricated structure has the capability to self-twist and contract, as an artificial muscle, with the increase of temperature and humidity. These impressive capabilities were even enhanced by introducing artificial nanomaterials (i.e., GNPs). The mechanical properties of the bimorph springs were investigated and tuned by the addition of GNPs. In view of the reported preliminary bio-safety assessment, the addition of GNPs does not significantly alter the biocompatibility of the used biopolymers. This latest result opens the applications of the herein presented 4D printed thermal and humidity-responsive structures as smart scaffolds for regenerative medicine or tools for intestinal surgery.

Supporting Information

Supporting Information is available from the Wiley Online Library or from the author.

Acknowledgements

anticlockwise and clockwise rotations at 37 and 25 °C, respectively. The PHBV-RS 80:20 formulation is not shown because no rotation was recorded. C) Rotation speed of the torsional actuation of the prepared springs. D) Proof of concept of bimorph spring as actuator in regenerative medicine application: photographs of the integration of PHBV-RS/GNPs 80:20 spring for distraction of the flaps of a phantom intestine. E) Setup used for measuring gauge force. F) Gauge force of the prepared springs under 90% RH as a function of time. After 20 min the samples were exposed to environmental conditions, that is, 25 °C and 35% RH, respectively.
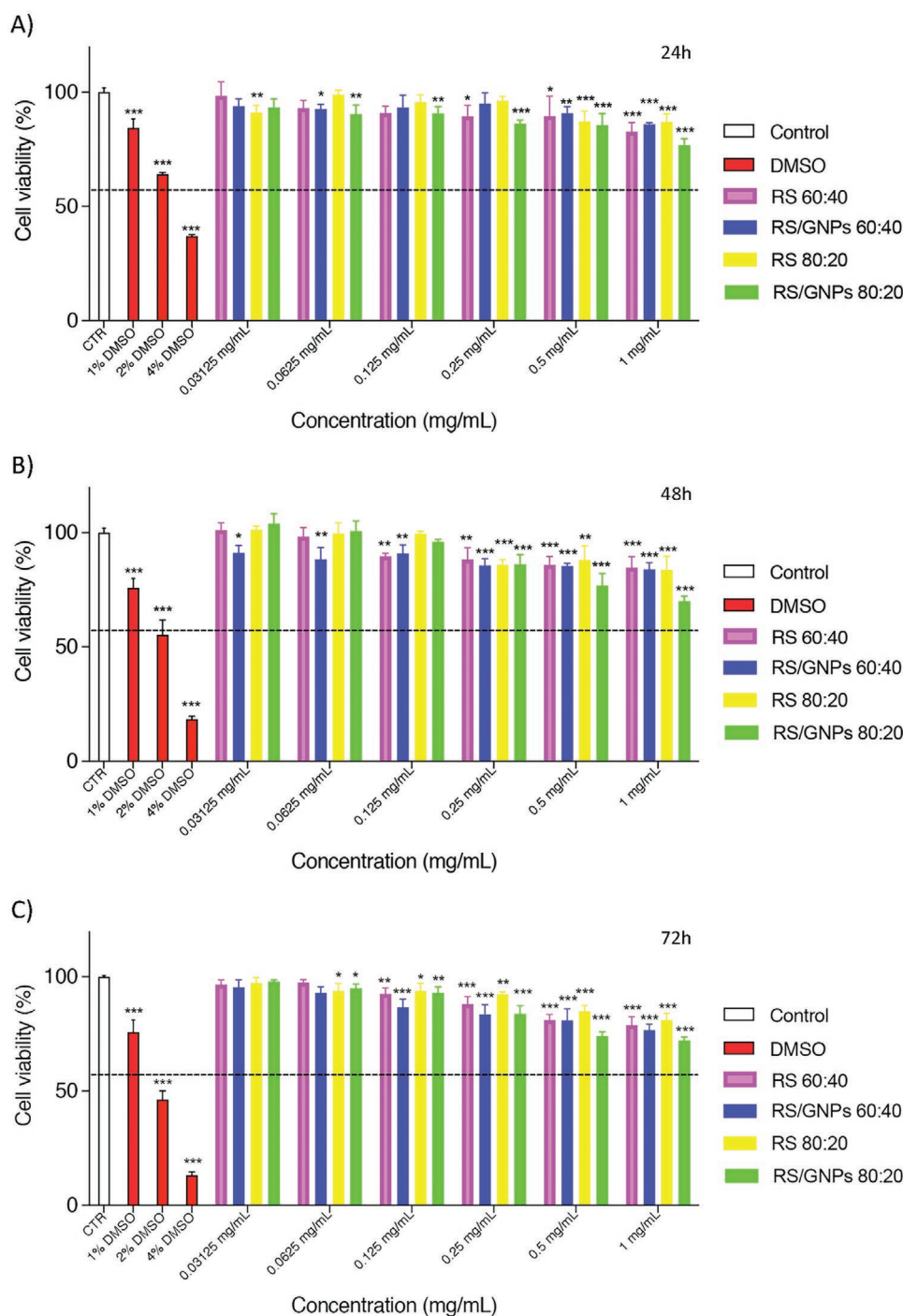
**ADVANCED
SCIENCE NEWS**

www.advancedsciencenews.com

**ADVANCED
FUNCTIONAL
MATERIALS**

www.afm-journal.de

Figure 9. Safety evaluation of the RS and RS/GNPs core compounds tested in vitro using MTT test. HepG2 cells were treated with six scalar concentrations for A) 24 h, B) 48 h and C) 72 h. The percentage of viable cells with respect to the control was reported as the mean standard deviation of three independent experiments, each conducted in triplicate. Positive controls were obtained with DMSO 1%, 2%, and 4%. *$p < 0.01$, **$p < 0.001$, and ***$p < 0.0001$, treatments versus Ctr (one-way ANOVA test).

Conflict of Interest

The authors declare no conflict of interest.

Data Availability Statement

Research data are not shared.

Keywords

[1] R. Elbaum, L. Zaltzman, I. Burgert, P. Fratzl, *Science* **2007**, *316*, 884.

[2] N. C. Grassly, C. Fraser, G. P. Garnett, *Nature* **2005**, *433*, 417.

[3] S. Armon, E. Efrati, R. Kupferman, E. Sharon, *Science* **2011**, *333*, 1726.

[4] S. J. Gerbode, J. R. Puzey, A. G. McCormick, L. Mahadevan, *Science* **2012**, *337*, 1087.

[5] C. G. Meloche, J. P. Knox, K. C. Vaughn, *Planta* **2007**, *225*, 485.

[6] A. J. Bowling, K. C. Vaughn, *Am. J. Bot.* **2009**, *96*, 719.

[7] M. Kanik, S. Orguc, G. Varnavides, J. Kim, T. Benavides, D. Gonzalez, T. Akintilo, C. C. Tasan, A. P. Chandrakasan, Y. Fink, P. Anikeeva, *Science* **2019**, *365*, 145.

[8] A. Maziz, A. Concas, A. Khaldi, J. Stålhand, N.-K. Persson, E. W. H. Jager, *Sci. Adv.* **2017**, *3*, e1600327.

[9] A. Lendlein, R. Langer, *Science* **2002**, *296*, 1673.

[10] J. Park, J. W. Yoo, H. W. Seo, Y. Lee, J. Suhr, H. Moon, J. C. Koo, H. R. Choi, R. Hunt, K. J. Kim, S. H. Kim, J.-D. Nam, *Smart Mater. Struct.* **2017**, *26*, 035048.

[11] C. S. Haines, N. Li, G. M. Spinks, A. E. Aliev, J. Di, R. H. Baughman, *Proc. Natl. Acad. Sci. U. S. A.* **2016**, *113*, 11709.

[12] C. S. Haines, M. D. Lima, N. Li, G. M. Spinks, J. Foroughi, J. D. W. Madden, S. H. Kim, S. Fang, M. J. de Andrade, F. Göktepe, Ö. Göktepe, S. M. Mirvakili, S. Naficy, X. Lepró, J. Oh, M. E. Kozlov, S. J. Kim, X. Xu, B. J. Swedlove, G. G. Wallace, R. H. Baughman, *Science* **2014**, *343*, 868.

[13] O. Kim, T. J. Shin, M. J. Park, *Nat. Commun.* **2013**, *4*, 2208.

[14] A. Lendlein, H. Jiang, O. Jünger, R. Langer, *Nature* **2005**, *434*, 879.

[15] K.-Y. Chun, S. H. Kim, M. K. Shin, C. H. Kwon, J. Park, Y. T. Kim, G. M. Spinks, M. D. Lima, C. S. Haines, R. H. Baughman, S. J. Kim, *Nat. Commun.* **2014**, *5*, 3322.

[16] M. D. Lima, N. Li, M. J. de Andrade, S. Fang, J. Oh, G. M. Spinks, M. E. Kozlov, C. S. Haines, D. Suh, J. Foroughi, S. J. Kim, Y. Chen, T. Ware, M. K. Shin, L. D. Machado, A. F. Fonseca, J. D. W. Madden, W. E. Voit, D. S. Galvão, R. H. Baughman, *Science* **2012**, *338*, 928.

[17] J. Deng, Y. Xu, S. He, P. Chen, L. Bao, Y. Hu, B. Wang, X. Sun, H. Peng, *Nat. Protoc.* **2017**, *12*, 1349.

[18] S. H. Kim, C. H. Kwon, K. Park, T. J. Mun, X. Lepró, R. H. Baughman, G. M. Spinks, S. J. Kim, *Sci. Rep.* **2016**, *6*, 23016.

[19] P. Chen, Y. Xu, S. He, X. Sun, S. Pan, J. Deng, D. Chen, H. Peng, *Nat. Nanotechnol.* **2015**, *10*, 1077.

[20] L. Moroni, T. Boland, J. A. Burdick, C. De Maria, B. Derby, G. Forgacs, G. Vozzi, *Trends Biotechnol.* **2018**, *36*, 384.

[21] I. Chiesa, C. Ligorio, A. F. Bonatti, A. De Acutis, A. M. Smith, A. Saiani, C. De Maria, *Front. Med. Technol.* **2020**, *2*, 571626.

[22] I. Chiesa, G. M. Fortunato, A. Lapomarda, L. Di Pietro, F. Biagini, A. De Acutis, G. Vozzi, *Int. J. Artif. Organs* **2019**, *42*, 586.

[23] N. Agarwal, D. A. Hoagland, R. J. Farris, *J. Appl. Polym. Sci.* **1997**, *63*, 401.

[24] S. B. Bon, I. Chiesa, D. Morselli, M. D. Esposti, P. Fabbri, C. De Maria, T. F. Viligiardi, A. Morabito, G. Giorgi, L. Valentini, *Mater. Des.* **2021**, *201*, 109492.

[25] C. Holland, K. Numata, J. Rnjak-Kovacina, F. P. Seib, *Adv. Healthcare Mater.* **2019**, *8*, 1800465.

[26] M. D. Esposti, F. Chiellini, F. Bondioli, D. Morselli, P. Fabbri, *Mater. Sci. Eng., C* **2019**, *100*, 286.

[27] F. R. Demehri, P. M. Wong, J. J. Freeman, Y. Fukatsu, D. H. Teitelbaum, *Pediatr. Surg. Int.* **2014**, *30*, 1223.

[28] F. R. Demehri, J. J. Freeman, Y. Fukatsu, J. Luntz, D. H. Teitelbaum, *Surgery* **2015**, *158*, 802.

[29] F. R. Demehri, J. J. Freeman, Y. Fukatsu, J. Luntz, D. H. Teitelbaum, *J. Pediatr. Surg.* **2016**, *51*, 101.

[30] L. S. Wood, H. S. Hosseini, M. Diyaolu, A.-L. Thomas, J. S. Taylor, J. C. Dunn, *J. Pediatr. Surg.* **2021**, *56*, 1192.

[31] X. Kuang, D. J. Roach, J. Wu, C. M. Hamel, Z. Ding, T. Wang, H. J. Qi, *Adv. Funct. Mater.* **2019**, *29*, 1805290.

[32] S. Tibbits, *Archit. Des.* **2014**, *84*, 116.

[33] M. Bodaghi, R. Noroozi, A. Zolfagharian, M. Fotouhi, S. Norouzi, *Materials* **2019**, *12*, 1353.

[34] S. Micalizzi, A. D. Lantada, C. De Maria, *Smart Mater. Struct.* **2019**, *28*, 105025.

[35] I. K. Schmolka, *J. Biomed. Mater. Res.* **1972**, *6*, 571.

[36] Midair 3D Printing: Making Coil Springs Without Support, https://makefastworkshop.com/hacks/?p=20181112 (accessed: May 2021).

[37] I. Chiesa, C. De Maria, A. Lapomarda, G. M. Fortunato, F. Montemurro, R. Di Gesù, R. Gottardi, *Biofabrication* **2020**, *12*, 025013.

[38] A. M. W. Bulte, E. M. Naafs, F. Van Eeten, M. H. V. Mulder, C. A. Smolders, H. Strathmann, *Polymer* **1996**, *37*, 1647.

[39] A. Antunes, A. Popelka, O. Aljarod, M. K. Hassan, P. Kasak, A. S. Luyt, *Polymers* **2020**, *12*, 1743.

[40] M. Acito, D. Bartolini, M. R. Ceccarini, C. Russo, S. Vannini, L. Dominici, M. Codini, M. Villarini, F. Galli, T. Beccari, M. Moretti, *Toxicol. In Vitro* **2020**, 10500.

[41] C. Pagano, L. Perioli, L. Latterini, M. Nocchetti, M. R. Ceccarini, M. Marani, D. Ramella, M. Ricci, *Appl. Clay Sci.* **2016**, *168*, 382.

[42] M. R. Ceccarini, S. Vannini, S. Cataldi, M. Moretti, M. Villarini, B. Fioretti, E. Albi, T. Beccari, M. Codini, *Biomed Res. Int.* **2016**, 7529521.

[43] C. S. O'Bryan, T. Bhattacharjee, S. R. Niemi, S. Balachandar, N. Baldwin, S. T. Ellison, T. E. Angelini, *MRS Bull.* **2017**, *42*, 571.

[44] X. Xia, J. Li, J. Zhang, G. J. Weng, *Int. J. Eng. Sci.* **2021**, *158*, 103411.

[45] Q. Xue, C. Lv, M. Shan, H. Zhang, C. Ling, X. Zhou, Z. Jiao, *Comp. Mater. Sci.* **2013**, *71*, 66.

[46] H. Ribeiro, W. M. Silva, M.-T. F. Rodrigues, J. C. Neves, R. Paniago, C. Fantini, H. D. R. Calado, L. M. Seara, G. G. Silva, *J. Mater. Sci.* **2013**, *48*, 7883.

[47] X. Hu, D. Kaplan, P. Cebe, *Macromolecules* **2006**, *39*, 6161.

[48] M. D. Basson, G. D. Li, F. Hong, O. Han, B. E. Sumpio, *J. Cell. Physiol.* **1996**, *168*, 476.

[49] S. G. Frangos, R. Knox, Y. Yano, E. Chen, G. Di Luozzo, A. H. Chen, B. E. Sumpio, *Endothelium* **2001**, *8*, 1.

[50] I. Agnarsson, A. Dhinojwala, V. Sahni, T. A. Blackledge, *J. Exp. Biol.* **2009**, *212*, 1990.

[51] T. A. Blackledge, C. Boutry, S. C. Wong, A. Baji, A. Dhinojwala, V. Sahni, I. Agnarsson, *J. Exp. Biol.* **2009**, *212*, 1980.

[52] K. Yazawa, K. Ishida, H. Masunaga, T. Hikima, K. Numata, *Biomacromolecules* **2016**, *17*, 1057.

[53] K. Yazawa, K. Ishida, H. Masunaga, T. Hikima, K. Numata, *Biomacromolecules* **2016**, *17*, 1057.

[54] Y. E. Kim, Y.-J. Kim, *Polym. J.* **2013**, *45*, 845.

[55] P. Kumar, V. Pillay, Y. E. Choonara, *Sci. Rep.* **2021**, *11*, 3104.

[56] S. Paolacci, M. R. Ceccarini, M. Codini, E. Manara, S. Tezzele, M. Percio, N. Capodicasa, D. Kroni, M. Dundar, M. C. Ergoren, T. Sanlidag, T. Beccari, M. Farronato, G. Farronato, G. M. Tartaglia, M. Bertelli, *Acta Biomed.* **2020**, *91*, e2020009.